# A NEW METHOD TO MEASURE THE POST-REIONIZATION IONIZING BACKGROUND FROM THE JOINT DISTRIBUTION OF LYMAN- $\alpha$ AND LYMAN- $\beta$ FOREST TRANSMISSION\*

FREDERICK B. DAVIES<sup>1</sup>, JOSEPH F. HENNAWI<sup>2,1</sup>, ANNA-CHRISTINA EILERS<sup>1,†</sup>, ZARIJA LUKIĆ<sup>3</sup>  $^{1}\text{Max-Planck-Institut für Astronomie, Königstuhl 17, D-69117 Heidelberg, Germany}$   $^{2}\text{Department of Physics, University of California, Santa Barbara, CA 93106, USA}$   $^{3}\text{Lawrence Berkeley National Laboratory, CA 94720-8139, USA}$   $^{3}\text{Draft version March 31, 2017}$ 

# ABSTRACT

The amplitude of the ionizing background that pervades the intergalactic medium (IGM) at the end of the epoch of reionization provides a valuable constraint on the emissivity of the sources which reionized the Universe. While measurements of the ionizing background at lower redshifts rely on a simulation-calibrated mapping between the photoionization rate and the mean transmission of the Ly $\alpha$  forest, at  $z \gtrsim 6$  the IGM becomes increasingly opaque, and transmission arises solely in narrow spikes separated by saturated Gunn-Peterson troughs. In this regime, the traditional approach of measuring the average transmission over large  $\sim 50~{\rm Mpc}/h$  regions is less sensitive and sub-optimal. Additionally, the five times smaller oscillator strength of the Ly $\beta$  transition implies the Ly $\beta$  forest is considerably more transparent at  $z \gtrsim 6$ , even in the presence of contamination by foreground  $z\sim5$  Ly $\alpha$  forest absorption. In this work we present a novel statistical approach to analyze the joint distribution of transmission spikes in the co-spatial  $z\sim 6~{\rm Ly}\alpha$  and  ${\rm Ly}\beta$  forests. Our method relies on Approximate Bayesian Computation (ABC), which circumvents the necessity of computing the intractable likelihood function describing the highly correlated Ly $\alpha$  and Ly $\beta$  transmission. We apply ABC to mock data generated from a large-volume hydrodynamical simulation combined with a state-of-the-art model of ionizing background fluctuations in the post-reionization IGM, and show that it is sensitive to higher IGM neutral hydrogen fractions than previous techniques. As a proof of concept, we apply this methodology to a real spectrum of a z = 6.54 quasar and measure the ionizing background from  $5.4 \le z \le 6.4$  along this sightline with  $\sim 0.2$  dex statistical uncertainties.

# 1. INTRODUCTION

Following the recombination of the Universe and the release of the cosmic microwave background (CMB), the vast majority of baryonic matter in the intergalactic medium (IGM) consisted of neutral atoms, in stark contrast to the highly ionized IGM seen a few billion years later (Gunn & Peterson 1965) and at the present day (Field 1959). The first stars, galaxies, and black holes are believed to be responsible for the intervening phase transition known as the epoch of reionization (Loeb & Furlanetto 2013). Through study of the reionization process, we hope to understand the nature of the faintest and earliest collapsed structures.

The CMB itself provides an "integral" constraint on the total column density of ionized gas through the measured optical depth to electron scattering  $\tau_e$ , and thus a characteristic reionization redshift  $z_{\rm reion} \sim 8$  (Planck Collaboration et al. 2016a). However, a wide range of models for the reionization history are consistent with CMB measurements (Planck Collaboration et al. 2016b), and  $\tau_e$  alone does not constrain the topology of the inho-

davies@mpia.de

mogeneous reionization process (Furlanetto et al. 2004). An important boundary condition to the epoch of reionization is the ubiquitous transmission through the Ly $\alpha$  forest at  $z\lesssim5.5$  which is inconsistent with a predominantly neutral IGM (e.g. McGreer et al. 2011, 2015). Large stretches of neutral gas are still possible at higher redshift  $z\gtrsim6$  where the Ly $\alpha$  forest is almost entirely opaque.

The  $z \sim 6$  Ly $\alpha$  forest has been studied for well over a decade to constrain the evolution of the ionization state of the Universe close to the reionization epoch (e.g. Becker et al. 2001; White et al. 2003; Songaila 2004; Fan et al. 2002, 2006). As shown by the data points in the second panel from the bottom of Figure 1, above  $z\sim5.5$ the typical opacity – and the typical variation between different lines of sight – increases rapidly. Eventually, the only transmission seen in the  $Lv\alpha$  forest is in narrow transmission spikes, likely corresponding to smallscale regions of the universe with particularly low density (e.g. Oh & Furlanetto 2005). The large-scale transmission measurements then simply reflect the number and strength of these spikes that fall into wide bins in each spectrum, where the size is defined either in terms of redshift interval ( $\Delta z \sim 0.15$ ; e.g. Fan et al. 2006) or by comoving distance (50 Mpc/h; Becker et al. 2015), both roughly corresponding to the scale of the first large-scale opaque regions, known as Gunn-Peterson troughs (after Gunn & Peterson 1965; henceforth GP troughs), observed in the spectra of z > 6 quasars (Fan et al. 2001; Becker et al. 2001; Fan et al. 2003; White et al. 2003). Indeed, some large-scale regions with formal limits on

<sup>\*</sup> Some of the data presented herein were obtained at the W.M. Keck Observatory, which is operated as a scientific partnership among the California Institute of Technology, the University of California and the National Aeronautics and Space Administration. The Observatory was made possible by the generous financial support of the W.M. Keck Foundation.

<sup>&</sup>lt;sup>†</sup> Fellow of the International Max Planck Research School for Astronomy and Cosmic Physics at the University of Heidelberg (IMPRS-HD).

their mean transmission contain high significance transmission spikes (Becker et al. 2015), which results in mean transmission below the significance threshold  $(2\sigma)$  when combined with surrounding GP troughs. Clearly, there is information in these small-scale transmission features which is lost when averaging on large scales, suggesting a "matched filtering" approach targeting transmission spikes would be more sensitive.

Another limiting factor for determining the ionization state of the  $z\gtrsim 6$  Universe is that the Ly $\alpha$  forest becomes essentially completely saturated, even at small scales, with many lines of sight consistent with zero transmission. The red dotted line in the bottom panels of Figure 1 shows the  $2\sigma$  limiting optical depth for 10 ks exposure time on a bright ( $F_{\rm cont}=10^{-17}~{\rm erg~s^{-1}~cm^{-2}}$ ) high-redshift quasar with a 10-meter telescope. The solid curves of the panel second from the bottom show the evolution of the Ly $\alpha$  forest opacity computed from the hydrodynamical simulation described in § 2 assuming different toy models for the evolution in the hydrogen ionization rate  $\Gamma_{\rm H\,I}$  and corresponding evolution in the volume-averaged hydrogen neutral fraction  $\langle x_{\rm HI} \rangle_V$  shown in the top panels.

The Ly $\beta$  forest saturates later because of its weaker oscillator strength,  $f_{\text{Ly}\beta}\lambda_{\text{Ly}\beta} \sim 0.16 f_{\text{Ly}\alpha}\lambda_{\text{Ly}\alpha}$  where  $f_i$  and  $\lambda_i$  are the oscillator strength and rest-frame wavelength of transition i, respectively. In practice the interpretation of Ly $\beta$  measurements is complicated by the presence of lower redshift Ly $\alpha$  absorption, which at  $z_{\text{Ly}\beta} \sim 6$  corresponds to  $z_{\rm Ly\alpha} \sim 5$ . Fortunately, the  $z \sim 5$  Ly $\alpha$  forest has relatively small scatter and is well-understood compared to the strong fluctuations seen at z > 5.5 (e.g. Becker et al. 2015) and its statistics can be modeled with standard simulations of the IGM that employ a uniform ionizing background. The bottom panel of Figure 1 shows similar curves to the panel above it, but computed for the Ly $\beta$  forest including the presence of foreground Ly $\alpha$ , demonstrating that observable Ly $\beta$  transmission should persist to substantially higher redshift than Ly $\alpha$ at fixed observational cost.

The most striking example of the increased sensitivity provided by Ly $\beta$  is the  $\sim 110~{\rm Mpc}/h$  GP trough observed in the z=5.98 quasar ULAS J0148+0600 with an effective optical depth  $\tau_{\rm eff}>7.4$  ( $2\sigma$  limit) in the Ly $\alpha$  forest, but which shows many prominent transmission spikes in the Ly $\beta$  forest (see Figure 5 in Becker et al. 2015). The presence of Ly $\beta$  transmission proves the existence of a highly-ionized IGM in this region despite the complete saturation of Ly $\alpha$ , consistent with theoretical predictions for large-scale fluctuations in the ionizing background after the end of reionization (Davies & Furlanetto 2016) or relic temperature fluctuations due to inhomogeneous heating during reionization (D'Aloisio et al. 2015; Davies et al., in prep.).

In this work, we present theoretical expectations for the distribution of  $\text{Ly}\alpha$  and  $\text{Ly}\beta$  forest transmission on varying  $\geq$ Mpc scales at  $z\sim 6$ , and demonstrate their ability to constrain the evolving ionizing background at high redshift. To account for sparseness, correlations, and extreme-value characteristics of potential data sets we apply a statistical method known as Approximate Bayesian Computation (ABC). ABC approximates the likelihood function through a massive Monte Carlo of mock data realizations, in contrast to more typical meth-

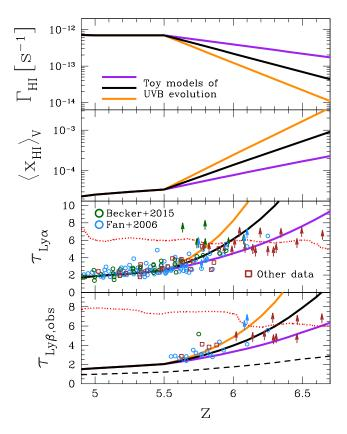


Figure 1. The top two panels show toy models for an evolving ionization rate  $\Gamma_{\rm H\,I}$  and the corresponding volume-weighted IGM neutral fraction  $(x_{\rm H\,I})_V$ . The bottom two panels show the 50 Mpc/h Ly $\alpha$  and Ly $\beta$  forest  $\tau_{\rm eff}$  measurements in Fan et al. (2006) and Becker et al. (2015) as the blue and green open circles, respectively, compared to simulated  $\tau_{\rm eff}$  (solid curves) corresponding to the ionizing background evolution models in the top panel. The brown squares show quasar measurements not present in the other compilations (Willott et al. 2007; Mortlock et al. 2009; Goto et al. 2011; Tang et al. 2016; Barnett et al. 2017) and observations of high-redshift gamma ray bursts (Chornock et al. 2013, 2014). Upward arrows represent  $2\sigma$  upper limits for measured transmission values that fall below reported  $2\sigma$  uncertainties. The dotted curve in the bottom two panels shows the  $2\sigma$  limiting effective optical depth on 50  $\mathrm{Mpc}/h$  scales for a simulated 10 ks Keck spectrum of a bright high-redshift quasar ( $F_{\text{cont}} = 10^{-17} \text{ erg s}^{-1} \text{ cm}^{-2} \text{ Å}^{-1}$ ). The long-dashed curve in the bottom panel shows the contribution of the foreground Ly $\alpha$  forest to the Ly $\beta$  forest  $\tau_{\rm eff}$ .

ods that assume a functional form (e.g. a multivariate Gaussian distribution). In § 2, we describe our numerical modeling of the Ly\$\alpha\$ and Ly\$\beta\$ forests and fluctuations in the ionizing background and present simulated distributions of Ly\$\alpha\$ and Ly\$\beta\$ forest transmission. In § 3, we describe our approach to measure the strength of the ionizing background using ABC. In § 4, we apply our statistical method to real data as a proof-of-concept test, providing (model-dependent) constraints on  $\Gamma_{\rm H\,I}$  at  $z\gtrsim5.5$  from a single high-redshift quasar spectrum. In § 5, we conclude with a summary and a discussion of predicted constraints from future samples of z>6 quasar spectra, where the addition of more quasars should both tighten the constraints on  $\Gamma_{\rm H\,I}$  and allow for constraints on the topology of ionizing background fluctuations.

All distance units are comoving unless specified otherwise. We assume a  $\Lambda$ CDM cosmology with  $\Omega_m = 0.3$ ,

 $\Omega_{\Lambda} = 0.7$ ,  $\Omega_b = 0.047$ , h = 0.685, and  $\sigma_8 = 0.8$ .

### 2. MODELING THE Ly $\alpha$ AND Ly $\beta$ FORESTS

In this section, we describe our method for modeling the Ly $\alpha$  and Ly $\beta$  forests in the spectrum of  $z \gtrsim 6$ quasars. Our physical model for the IGM is a cosmological hydrodynamical simulation using the Nyx code (Almgren et al. 2013; Lukić et al. 2015), 100 Mpc/h on a side, with 4096<sup>3</sup> dark matter particles and 4096<sup>3</sup> baryon fluid cells. We use outputs of the density, temperature, and velocity fields at z = 6.0 and z = 5.0 to model the  $z \sim 6 \text{ Ly}\alpha$  and  $\text{Ly}\beta$  forest and the  $z \sim 5 \text{ Ly}\alpha$  contamination of the  $z \sim 6$  Ly $\beta$  forest, respectively. We extract random skewers from these simulation outputs, compute the H I fraction in every cell assuming ionization equilibrium, and then calculate Ly $\alpha$  and Ly $\beta$  transmission along the line of sight including the effects of peculiar motions and thermal broadening (see Lukić et al. 2015 for more details). We re-scale the physical gas density along each skewer by  $(1+z)^3$  to account for cosmological expansion, making the simplifying assumption that within the redshifts of interest the evolution of the overdensity field is less important.

Our simulation meets the suggested mass resolution requirement to resolve the z=5 Ly $\alpha$  forest proposed by Bolton & Becker (2009) ( $M_{\rm gas}\lesssim 3\times 10^5~{\rm M}_{\odot}$ ), although convergence may be different for a grid code like Nyx versus the smoothed-particle hydrodynamics (SPH) simulations they studied. Convergence may also be more difficult for the extremely low transmission of the  $z \gtrsim 6$ Ly $\alpha$  forest, suggested by the lack of convergence between the co-spatial Ly $\alpha$  and Ly $\beta$  optical depths at  $z \sim 6$  of relatively high-resolution simulations shown in the Appendix of Becker et al. (2015). In future work we will quantify the convergence (or lack thereof) of the  $z \gtrsim 6$ IGM in our simulation, extending the tests in Lukić et al. (2015) which were limited to  $z \leq 4$ , but preliminary tests suggest that the mean Ly $\alpha$  transmission is converged to better than  $\sim 10\%$  (J. Oñorbe, private communication). We note that the convergence of the  $z = 5-6 \text{ Ly}\alpha$  forest is assisted by the non-adaptive spatial resolution of the Eulerian grid in the most underdense environments which lead to Ly $\alpha$  forest transmission (Oh & Furlanetto 2005) (as opposed to, e.g., nearest-neighbor smoothing kernels in SPH codes).

We include noise in our mock spectra using a noise vector extracted from a spectrum of the  $z \sim 6.4$  quasar SDSS J1148+5251 taken with the Echellete Spectrograph and Imager (ESI; Sheinis et al. 2002) on the Keck II telescope with a total exposure time of 13,200s (PI: Cowie), re-scaled to an effective exposure time of 10,000s by multiplying the noise by  $\sqrt{13200/10000} \sim 1.15$ . The noise vector includes contributions from read noise, sky noise, and the varying sensitivity of ESI as a function of wavelength. We assume that the noise is independent and Gaussian-distributed in each pixel and that the presence of source signal does not affect the noise level, a good assumption for the faint  $z \gtrsim 6$  quasars for which the sky background dominates the noise budget. The quasar spectrum is assumed to follow the composite spectrum of Lusso et al. (2015) assuming a flux density at 1450Å of  $F_{\lambda}(1450\text{Å}) = 10^{-17} \text{ erg s}^{-1} \text{ cm}^{-2} \text{Å}^{-1}$ , corresponding to a fairly bright  $z \sim 6$  quasar with  $M_{1450} \sim -27$ .

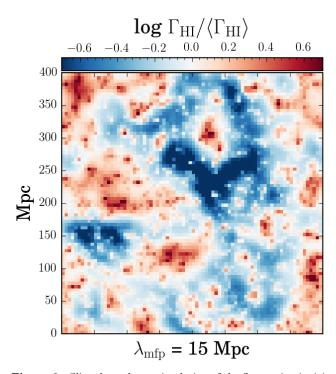


Figure 2. Slice through our simulation of the fluctuating ionizing background at z=6 computed as in Davies & Furlanetto (2016) with the mean free path at the average strength of the ionizing background fixed to 15 Mpc. Strong large-scale fluctuations exist on  $\sim 100$  Mpc scales as required by observations of Gunn-Peterson troughs at  $z \gtrsim 5.5$  (Fan et al. 2006; Becker et al. 2015).

We model fluctuations in the post-reionization ionizing background in a separate (400 Mpc)<sup>3</sup> cosmological volume using the method of Davies & Furlanetto (2016, henceforth DF16). We defer the interested reader to DF16 for the details, but we briefly summarize the method here. We use the semi-numerical simulation code DEXM (Mesinger & Furlanetto 2007) to generate a realization of cosmological initial conditions in a  $(400 \text{ Mpc})^3$ volume and populate it with dark matter halos down to  $M_{\rm h,min} = 2 \times 10^9 \ M_{\odot}$  following the excursion set formalism. We then abundance match these halos to the measured Bouwens et al. (2015)  $z \sim 6$  rest-frame UV luminosity function of galaxies down to absolute magnitudes of  $M_{\rm UV,max} \sim -12.5$ , and assume a constant ratio between the non-ionizing UV luminosity and the (escaping) ionizing luminosity of each galaxy. The ionizing background from these galaxies is computed on a coarse 80<sup>3</sup> grid allowing the mean free path of ionizing photons to vary spatially depending on the large-scale density field and local ionizing background,  $\lambda \propto \Gamma_{\rm H\,I}^{2/3} \Delta^{-1}$ , with the average mean free path in the volume normalized to  $\lambda_{\rm mfp}=15$  Mpc. In Figure 2 we show a slice through the ionizing background model, which exhibits strong large-scale fluctuations consistent with what is required to reproduce the distribution of Gunn-Peterson troughs in the  $z \gtrsim 5.5 \text{ Ly}\alpha$  forest (DF16).

We simulate the ionizing background in a separate volume from the hydrodynamical simulation because the latter is not large enough to fully model the effect of the fluctuating mean free path of ionizing photons, and thus would have much weaker ionizing background fluctuations on the  $\sim 100$  Mpc scales we investigate in this

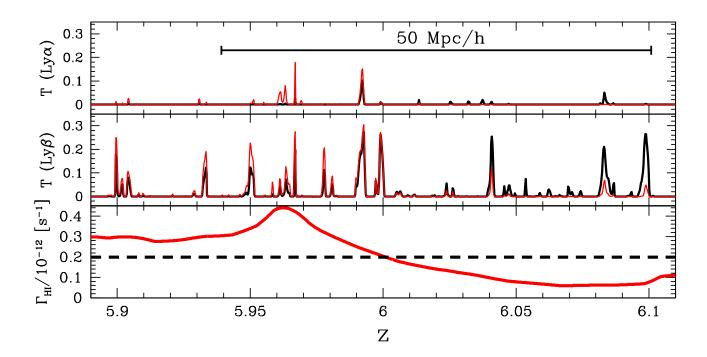


Figure 3. The top and middle panels show mock (noiseless) Ly $\alpha$  and Ly $\beta$  forest spectra, respectively, at  $z \sim 6$ . The black curve assumes a uniform ionization rate  $\Gamma_{\rm H\,I} = 10^{-12.7}~{\rm s}^{-1}$ , the dashed curve in the bottom panel, while the red curve demonstrates the effect of a fluctuating ionizing background skewer shown by the solid red curve in the bottom panel. In the upper panel we show a bar corresponding to the typical scale of mean transmission measurements (50 Mpc/h) in the Ly $\alpha$  forest from the literature (e.g. Fan et al. 2006; Becker et al. 2015).

work (DF16). Because of this, we are explicitly ignoring the anti-correlation of the density and radiation fields on very large scales shown by DF16. In this work we assume that this large-scale anti-correlation does not strongly affect the statistics of small-scale transmission features in the IGM, an assumption we will test in future work.

In the top and middle panels of Figure 3, we show Ly $\alpha$  and Ly $\beta$  forest segments of a mock spectrum from z = 5.9-6.1. As expected, the Ly $\beta$  forest shows considerably more transmission, and despite contamination by foreground  $z \sim 5 \text{ Ly}\alpha$  forest absorption, transmission features in the Ly $\alpha$  forest tend to show counterparts in the Ly $\beta$  forest. The red curves show the effect of applying the fluctuating ionizing background skewer in the bottom panel. Small-scale features in the Ly $\alpha$  forest are sensitive to ionizing background fluctuations because the optical depth in each pixel changes as  $\tau_{\alpha} \propto \Gamma_{\rm H\,I}^{-1}$ . The Ly $\beta$  forest is less sensitive to these fluctuations because  $\tau_{\beta}$  contains a constant factor from the foreground Ly $\alpha$ forest contamination which sets a floor to the opacity, i.e.  $\tau_{\beta} = \tau_{\beta,z\sim 6} + \tau_{\alpha,z\sim 5}$  where only the first term responds to  $z \sim 6$  background fluctuations<sup>1</sup>.

# 2.1. Ly $\alpha$ and Ly $\beta$ Transmission PDF on 2 & 20 Mpc Scales

 $^1$  In this work we assume that the ionizing background at  $z\sim 5$  is uniform, a reasonable assumption given the relatively large measured mean free path of ionizing photons (Worseck et al. 2014, but see D'Aloisio et al. 2016) and the agreement between the distribution of large-scale Ly $\alpha$  forest optical depth with standard hydrodynamical simulations (Becker et al. 2015).

In the upper left set of panels in Figure 4 we show the transmission probability distribution function (PDF) on 2 Mpc scales (dz  $\sim 0.005$ ) of the Ly $\alpha$  and Ly $\beta$  forests from simulations of  $z\sim 6$  spectra with varying uniform  $\Gamma_{\rm H\,I}$  of  $10^{-12.4}~{\rm s}^{-1}$  (top, blue),  $10^{-12.7}~{\rm s}^{-1}$  (middle, black), and  $10^{-13.0}~{\rm s}^{-1}$  (bottom, orange). These  $\Gamma_{\rm H\,I}$  values roughly correspond to the mean and  $+/-1\sigma$  uncertainty range of current measurements from the Ly $\alpha$  forest at  $z \sim 6$  (Wyithe & Bolton 2011). The PDFs are characterized by a Gaussian peak around zero – corresponding to the noise floor, shown as the dotted line in every panel - and a tail towards higher transmission whose steepness is a function of ionizing background strength. The shape of the PDF is markedly different from the distributions seen at  $z \sim 2-3$  (e.g. Lee et al. 2015) because the  $z \gtrsim 6 \text{ Ly}\alpha$  and Ly $\beta$  forests are so opaque that they almost never come close to the continuum (see also Becker et al. 2007). In the bottom panels the red curve corresponds to a model with the same average  $\Gamma_{\rm H\,I}=10^{-12.7}$ s<sup>-1</sup> that includes fluctuations in the ionizing background (as shown in Figures 2 and 3). In general the effect of background fluctuations on the 2 Mpc-binned transmission PDF is minor, although it does lead to an extended tail of rare transmission spikes. The effect is larger on the Ly $\alpha$  PDF than the Ly $\beta$  PDF due to the contamination of Ly $\beta$  by foreground  $z \sim 5$  Ly $\alpha$  forest absorption, i.e., even if  $\Gamma_{\rm H\,I}$  fluctuates high, the transmission spikes can only increase up to the absorption level of the  $z\sim 5$ Ly $\alpha$  forest (§ 2).

In the right set of panels in Figure 4 we show the PDFs on 20 Mpc scales. This is analogous to previous studies

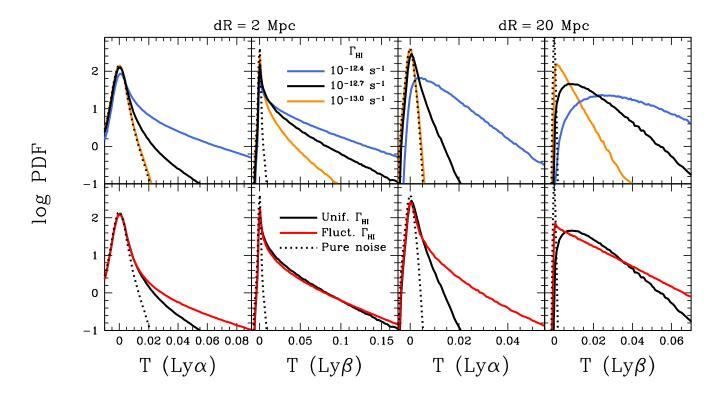


Figure 4. Simulated PDFs of 2 Mpc (left four panels) and 20 Mpc (right four panels) binned segments of the Ly $\alpha$  (left panels inside each dR) and Ly $\beta$  (right panels inside each dR) forests at  $z\sim 6$ . The upper panels show the variation in the PDFs as a function of the (uniform) ionization rate  $\Gamma_{\rm H\,I}=10^{-13.0}$ ,  $10^{-12.7}$ , and  $10^{-12.4}$  s<sup>-1</sup> as the orange, black, and blue curves, respectively. The lower panels show the effect of including fluctuations in the ionizing background (red curve) with an average  $\Gamma_{\rm H\,I}=10^{-12.7}$  s<sup>-1</sup>. The dotted curve in every panel shows the PDF of the noise model, which assumes independent Gaussian-distributed noise according to a noise vector from a real Keck/ESI spectrum.

of large bins in the Ly $\alpha$  forest (Fan et al. 2006; Becker et al. 2015) but at a scale smaller by around a factor of three. The distributions are narrower (note the difference in transmission scale on the horizontal axis), reflecting not only a decrease in sky noise (S/N  $\propto N_{\rm pix}^{-1/2}),$ but also the tendency for several transmission spikes to fall into a single bin leading to a somewhat more Gaussian shape to the distribution (as per the central limit theorem). For moderate ionization rates  $\Gamma_{\rm H\,I}\gtrsim 10^{-12.7}$  s<sup>-1</sup>, the model PDFs suggest that high signal-to-noise transmission should nearly always be measured in the  $Lv\beta$  forest at this scale. The effect of ionizing background fluctuations on the PDFs is considerably stronger on large scales, consistent with the  $\gtrsim 10$ s of Mpc typical scales of background fluctuations seen in the simulations (e.g. Figure 3). In particular the large-scale Ly $\beta$ PDF is strongly affected by ionizing background fluctuations through an excess in 20 Mpc-scale Ly $\beta$  -dark regions (GP troughs) over the uniform background model, which are otherwise consistent with the noise floor in the Ly $\alpha$  forest, suggesting that it may have considerable constraining power for the parameters of models for strong fluctuations in IGM opacity (e.g. DF16, D'Aloisio et al. 2015). The 20 Mpc-scale PDFs shown here are analogous to the 50 Mpc/h-scale (cumulative) PDFs studied by Becker et al. (2015) – they similarly allow one to characterize fluctuations in the Ly $\alpha$  and Ly $\beta$  forests on the large-scales expected from an inhomogeneous reioniza-

tion process (e.g. Furlanetto et al. 2004).

From these PDFs we should be able to assess the probability for any given model to reproduce rare transmission spikes in the Ly $\alpha$  and Ly $\beta$  forests, and from their detailed shape, study the patchy nature of the post-reionization IGM. In practice, performing parameter inference from the PDFs is difficult because much of their constraining power lies in a handful of transmission spikes in the tail of the distribution, and the features in the Ly $\alpha$  and Ly $\beta$  forests should be correlated because they trace the same physical structures.

# 3. STATISTICAL METHODS: APPROXIMATE BAYESIAN COMPUTATION

The standard approach to IGM parameter inference from the transmission PDF of the Ly $\alpha$  forest at  $z\sim 2$ –3 (e.g. Lidz et al. 2006) is to choose a set of coarse bins in the range of 0 < F < 1, compute the covariance matrix of the bins from either jackknife sampling of real data (Lidz et al. 2006; Lee et al. 2015) or forward-modeling of the Ly $\alpha$  forest in hydrodynamical simulations (Rollinde et al. 2013), and then approximate the likelihood function as a multivariate Gaussian. Because each PDF bin typically contains thousands of pixels, the central limit theorem ensures that a multivariate Gaussian likelihood is a good approximation.

The situation changes dramatically at higher redshifts where the IGM is more opaque and fewer quasars are available. At  $z \gtrsim 6$ , most pixels in the Ly $\alpha$  and Ly $\beta$ 

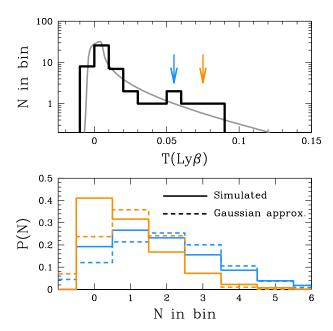


Figure 5. Top: The histogram shows the  $\Delta T=0.01$ -binned transmission distribution of a single mock observation of the Ly $\beta$  forest covering 100 Mpc with transmission binned on 2 Mpc scales, with  $\Gamma_{\rm H\,I}=10^{-12.7}~{\rm s}^{-1}$  and  $\lambda_{\rm mfp}=15$  Mpc at  $z\sim5.9$ –6.1. The curve shows the model PDF convolved with a  $\Delta T=0.01$  boxcar filter to be consistent with the binned PDF. Bottom: The solid and dashed histograms represent the true and Gaussian approximations to the distribution of PDF values, respectively. The two sets of histograms represent the two bins labeled (and color-coded) by the arrows in the top panel.

forests are consistent with zero transmission, with only a sparse tail of real transmission spikes. While the (co)variances of each bin can be estimated by forward modeling of mock spectra, the resulting Gaussian distributions (as defined by the mean and (co)variance of the mock samples) are not representative of the distributions of the number of pixels that fall into each bin. We show an example of this in Figure 5, where the bottom panel illustrates the true and Gaussian-approximated distributions of mock Ly $\beta$  PDF measurements in transmission bins highlighted in the top panel, with one mock observation shown.

The requirement of approximately Gaussian likelihood is more stringent for transmission measurements on larger bin scales, such as the  $50~{\rm Mpc}/h$  measurements by Becker et al. (2015), where the small number of measurements – and the tendency for measurements to be reported as limits – have typically led to rough "chiby-eye" comparisons to simulations (e.g. D'Aloisio et al. 2015; Davies & Furlanetto 2016; D'Aloisio et al. 2016).

To circumvent these challenges, we adopt the statistical approach known as ABC (e.g. Pritchard et al. 1999; see also Cameron & Pettitt 2012; Ishida et al. 2015; Hahn et al. 2016; Jennings & Madigan 2016 for other astronomical applications) which allows for parameter inference without any explicit analytic form for the likelihood function. We start with an abridged statement of Bayes' Theorem,

$$p(\theta|\mathbf{d}) \propto p(\mathbf{d}|\theta)p(\theta),$$
 (1)

where  $\theta$  represents the set of model parameters (e.g.  $\Gamma_{\rm H\,I}$ ) and **d** represents the data (e.g. the transmission

measured in each spectral pixel),  $p(\mathbf{d}|\theta)$  is the likelihood function,  $p(\theta)$  is the prior distribution representing our previous knowledge of the model parameters, and  $p(\theta|\mathbf{d})$  is the posterior distribution for  $\theta$  that we hope to obtain. In many cases, the likelihood function can be approximated as a multivariate Gaussian distribution or can be straightforwardly computed numerically, allowing the posterior distribution to be computed through methods such as Markov Chain Monte Carlo (MCMC). In our case, as we have shown above, such an approximation fails to adequately describe the distribution of mock measurements in our models.

One could imagine a brute force computation of the likelihood function by computing mock data sets to determine the probability of exactly reproducing the data, but this is computationally intractable for many problems. The first and most fundamental approximation proposed by ABC is to slightly blur the definition of the likelihood function, instead describing the posterior distribution as (e.g. Marin et al. 2012)

$$p(\theta|\mathbf{d}) \approx p_{\text{ABC}}(\theta|\mathbf{d}) \propto \int p(\rho(\mathbf{d}, \mathbf{x}) < \epsilon, \mathbf{x}|\theta) p(\theta) d\mathbf{x},$$
 (2)

where  $\mathbf{x}$  is a forward-modeled mock data set,  $\rho(\mathbf{d}, \mathbf{x})$  represents a distance measure between the data and mock data,  $\epsilon$  is a small tolerance threshold, and the integral is performed over the space of forward-modeled mock datasets. That is, to approximate the likelihood function, ABC proposes that coming *close* to the measured data is "good enough," allowing for far easier computation than the brute force method mentioned above. In the process, the correlations between data elements are naturally accounted for through the forward-modeling procedure without any explicit computation of the covariance matrix.

The simplest application of ABC in practice is to draw model parameter samples  $\theta^*$  from the prior, forward model a mock realization of the data given by those parameters  $\mathbf{x}^*$ , then measure the distance between the mock data and real data  $\rho(\mathbf{d}, \mathbf{x}^*)$ . If this distance is "small enough", i.e.  $\rho(\mathbf{d}, \mathbf{x}^*) < \epsilon$ , then  $\theta^*$  is accepted as a sample of the posterior distribution. This procedure is called ABC rejection sampling.

The above methodology may still be computationally intractable if the data represent a highly stochastic process or high-dimensional data set. For example, in our case, producing a mock data set that nearly matches an observed Ly $\alpha$  and/or Ly $\beta$  forest spectrum at the pixelto-pixel level (i.e. with small  $\rho(\mathbf{d}, \mathbf{x})$ ) requires nearly matching the peak heights and positions of every narrow transmission feature. In practice this would require matching not only the ionization state of the gas, but also the entire set of cosmological initial conditions that led to the structures observed along the sightline. To overcome this computational hurdle, the technique commonly employed in ABC is to use "summary statistics" to process the data (and mock data) into a form which allows them to be compared more easily, typically into a lowerdimensional state. This reformulation can be stated as

$$p(\theta|\mathbf{d}) \approx p(\theta|\mathbf{s}_{\text{obs}})$$

$$\approx p_{\text{ABC}}(\theta|\mathbf{s}_{\text{obs}}) \propto \int p(\rho(\mathbf{s}_{\text{obs}}, \mathbf{s}) < \epsilon, \mathbf{x}|\theta) p(\theta) d\mathbf{x}, (3)$$

where  $s_{\rm obs}$  is the summary statistic of the data and s is the summary statistic of mock data set x. If the summary statistic is "sufficient" then no information is lost, but such summary statistics are only known analytically in very simple cases (e.g., for determining the mean of a normally-distributed quantity, the sample mean is a sufficient statistic). Thus, in most cases, the use of a summary statistic implies loss of information, leading to bias and/or loss of precision in the posterior distribution. In § 3.2, we perform inference tests on multiple summary statistics of the Ly $\alpha$  and Ly $\beta$  forests to investigate their potential biases.

While ABC may seem like a "silver bullet" to perform parameter inference with the least number of assumptions about the nature of the likelihood function, its primary weakness is the requirement of simulating an overwhelmingly large number of mock data sets in order to produce a reasonably converged approximation to the posterior PDF. Even with a one-dimensional summary statistic one may have to generate millions of mock data sets, limiting its potential application for practical reasons. Nevertheless, ABC allows for inference involving complicated likelihood functions, fully accounting for covariance (depending on the sufficiency of the chosen summary statistic) implicitly as they manifest in the assumed model for mock data.

# 3.1. Application of ABC to the Ly $\alpha$ and Ly $\beta$ forests

Application of ABC to inference of the Ly $\alpha$  and Ly $\beta$  forests is performed as follows:

- 1. Draw a value of  $\Gamma_{\rm H\,I}$  from prior distribution,  $\Gamma_{\rm H\,I}^*$ .
- 2. Compute mock spectrum of Ly $\alpha$  and Ly $\beta$  forest with  $\Gamma_{\rm H\,I} = \Gamma_{\rm H\,I}^*$ , including noise consistent with observations.
- 3. Compute summary statistic of mock and observed spectra ( $\mathbf{s}$  and  $\mathbf{s}_{\mathrm{obs}}$ , respectively).
- 4. Compute distance between  $\mathbf{s}_{obs}$  and  $\mathbf{s}$ ,  $\rho(\mathbf{s}_{obs}, \mathbf{s})$ .
- 5. If  $\rho(\mathbf{s}_{\text{obs}}, \mathbf{s})$  is below the threshold  $\epsilon$ , keep  $\Gamma_{\text{H\,I}}^*$  as a sample of the approximate posterior PDF,  $p_{\text{ABC}}(\Gamma_{\text{H\,I}})$ .
- 6. Repeat steps 1–5 until a predetermined number of posterior PDF samples have been drawn, e.g. 1000.

In practice, the  $\Gamma^*_{\rm H\,I}$  can be drawn more efficiently, and in later sections we adopt a method based on importance sampling with an iteratively declining threshold  $\epsilon$  set based on percentiles of the distribution of  $\rho(\mathbf{s}_{\rm obs},\mathbf{s})$  (Beaumont et al. 2009; see detailed implementations by e.g. Ishida et al. 2015; Hahn et al. 2016; Jennings & Madigan 2016). These procedures are simply methods to increase the efficiency of the basic rejection sampling method, and as such we will not discuss them in further detail.

For a given segment of the Ly $\alpha$  or Ly $\beta$  forest, perhaps the most basic summary statistic is the mean transmission:  $\langle F \rangle = \sum_{i}^{N_{\rm pix}} F_i/N_{\rm pix}$ . The use of this statistic reduces the dimensionality of the data from [# of Ly $\alpha$  forest pixels + # of Ly $\beta$  forest pixels] to 2: the mean transmission in Ly $\alpha$  and the mean transmission in Ly $\beta$ .

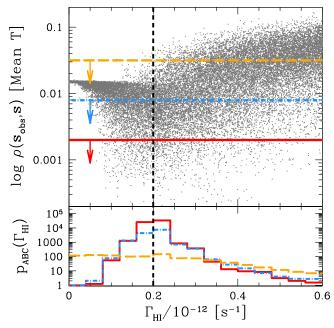


Figure 6. Demonstration of ABC applied to a mock observation of the Lyα and Lyβ forests. The "observation" consists of the mean transmissions of Lyα and Lyβ in a single mock spectrum covering 100 Mpc at  $z\sim 6$  with a fluctuating ionizing background and  $\Gamma_{\rm H\,I}=10^{-12.7}~\rm s^{-1}$ . The points in the upper panel represent the distances between the "observed" mock spectrum and 25000 additional mock spectra with  $\Gamma_{\rm H\,I}$  drawn from a uniform prior, where the distance has been defined using the mean transmission as the summary statistic (equation 4). The thick dashed orange, dot-dashed blue, and solid red histograms in the lower panel represent the ABC posterior distributions assuming thresholds of log  $\epsilon=$ -1.5, -2.1, and -2.7, respectively, corresponding to the horizontal lines in the upper panel.

That is,  $\mathbf{s} = (\langle F_{\mathrm{Ly}\alpha} \rangle, \langle F_{\mathrm{Ly}\beta} \rangle)$ . Using ABC, we do not have to make any assumptions about the nature of the intrinsic distributions of  $\mathrm{Ly}\alpha$  and  $\mathrm{Ly}\beta$  mean transmission, nor the details of their correlations. Instead, the process of comparison to forward modeled mock data naturally accounts for correlations under the assumption that our model for the IGM and the noise model of the spectrum is accurate.

We set up an example of the ABC procedure as follows. One mock data set with known  $\Gamma_{\rm H\,I}$ , specifically a noisy realization of the Ly $\alpha$  and Ly $\beta$  forest with fluctuating  $\Gamma_{\rm H\,I}$  shown in Figure 3, covering a path length of 100 Mpc, is chosen to be the "observed" sample. We then draw  $\Gamma_{\rm H\,I}^*$  from a uniform prior covering 0– $0.6 \times 10^{-12}$  s<sup>-1</sup>, forward model a mock data set using that  $\Gamma_{\rm H\,I}^*$ , then compute the distance between the observed and mock data sets.

$$\rho(\mathbf{s}_{\text{obs}}, \mathbf{s}) = \sqrt{(\langle F_{\text{obs}}^{\alpha} \rangle - \langle F_{\text{mock}}^{\alpha} \rangle)^2 + (\langle F_{\text{obs}}^{\beta} \rangle - \langle F_{\text{mock}}^{\beta} \rangle)^2}, \quad (4)$$

where we have adopted the  $L_2$  norm for the distance  $\rho$ . The result of such a test with 25000 mock data sets is shown in Figure 6. Each point in the top panel represents the distance defined above for a single mock spectrum corresponding to a draw of  $\Gamma_{\rm H\,I}^*$ , a random IGM skewer from the hydrodynamical simulation, and a random fluctuating ionizing background skewer. The bottom panel

shows binned samples from the posterior distribution of  $\Gamma_{\rm H\,I}$  obtained by rejecting samples with distance greater than the  $\epsilon$  values given by the horizontal lines in the upper panel (i.e. the samples below the lines are accepted). As the tolerance  $\epsilon$  is decreased, the ABC posterior distribution narrows, representing successive improvements to the approximated likelihood as it converges to the true distribution. Through the ABC process, this posterior distribution explicitly includes cosmic variance (as modeled by the cosmological simulation), measurement uncertainty, and the correlation between the Ly $\alpha$  and Ly $\beta$  forest mean transmissions.

However, the mean transmissions in the Ly $\alpha$  and Ly $\beta$ forests clearly do not tell the entire story. Due to sky noise, a large region of forest may have a mean transmission consistent with zero but still contain a significant positive spike (e.g. Figure 2 in Becker et al. 2015). The presence of any (real) transmission spike requires an ionizing background greater than zero, but the mean transmission alone may not contain this information because of limited signal-to-noise. A summary statistic which retains this information but disregards the locations of transmission spikes is the rank-order distribution of transmission on small scales. That is, a re-ordering of the transmission values such that they are in order from lowest to highest transmission. The scale over which the transmission is binned can be chosen to maximize the signal-to-noise ratio of transmission spikes, i.e. matched filtering. We also account for the spatially-varying noise of the spectrum (e.g. due to sky lines) by first dividing each transmission value by the local noise before reordering the measurements. An example of rank-order distributions of two mock Ly $\alpha$  forest spectra with the same  $\Gamma_{\rm H\,I}$  is shown in Figure 7. The distance between observed and mock data is then

$$\rho(\mathbf{s}_{\text{obs}}, \mathbf{s}) = \sqrt{\sum_{i}^{N_{\alpha}} (S_{i, \text{obs}}^{\alpha} - S_{i, \text{mock}}^{\alpha})^2 + \sum_{i}^{N_{\beta}} (S_{i, \text{obs}}^{\beta} - S_{i, \text{mock}}^{\beta})^2}, (5)$$

where  $S_i$  is the signal-to-noise ratio of the transmission in the bin with rank i (where the Ly $\alpha$  and Ly $\beta$  forests are ranked independently), and  $N_{\alpha}$  and  $N_{\beta}$  are the number of bins in the Ly $\alpha$  and Ly $\beta$  forests, respectively.

In Figure 8 we show a 2 Mpc-binned mock Ly $\alpha$  and Ly $\beta$  forest spectrum at  $z \sim 6.5$  with a fluctuating ionizing background and true  $\Gamma_{\rm H\,I} = 10^{-12.95}~{\rm s}^{-1}$ . The mean transmissions in Ly $\alpha$  and Ly $\beta$  are consistent with zero, but there is a highly significant (S/N>5) transmission spike in the Ly $\beta$  forest. In Figure 9 we show posterior PDFs for  $\Gamma_{\rm H\,I}$  using several different summary statistics. The blue and red curves shows the posterior PDF using the mean transmission and the 20 Mpc-binned rank-order distribution as summary statistics, both of which fail to measure  $\Gamma_{\rm H\,I}$ , i.e. the posterior PDF does not rule out  $\Gamma_{\rm H\,I}=0$ . In contrast, using the 2 Mpc-binned rank-order distribution as the summary statistic (black curve) allows for an actual measurement of  $\Gamma_{\rm H\,I}$ , demonstrating the enhanced ability of small-scale transmission features to constrain  $\Gamma_{\rm H\,I}$  relative to the large-scale mean.

As an example of the flexibility of the ABC procedure, the dotted curve in Figure 9 shows the posterior PDF from adopting a summary statistic that *com*-

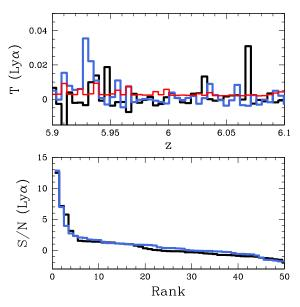


Figure 7. Top: Two mock Ly $\alpha$  forest spectra (black, blue) at  $z\sim 6$  computed with the same ionization rate  $\Gamma_{\rm H\,I}=10^{-12.6}~{\rm s}^{-1}$  and binned to 2 Mpc. The noise vector is shown as the red curve. Bottom: Rank-order distribution of the 2 Mpc binned signal-tonoise of the spectra shown in the upper panel. The "distance" between the two spectra, qualitatively the amount of "space" between the black and blue curves, is much smaller when arranged in rank order.

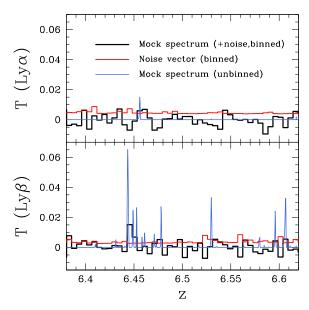


Figure 8. Top panels: Mock Ly $\alpha$  and Ly $\beta$  forest spectra (2 Mpc binned: black, noiseless unbinned: blue) and  $1\sigma$  noise (2 Mpc binned, red) for  $\Gamma_{\rm H\,I}=10^{-12.95}~{\rm s}^{-1}$  at  $z\sim6.5$ . The mean transmissions of Ly $\alpha$  and Ly $\beta$  are consistent with zero, but there is a highly significant transmission spike in the Ly $\beta$  forest which should definitively rule out  $\Gamma_{\rm H\,I}=0$ .

bines the 2 Mpc and 20 Mpc rank-order distributions by adding their distances in quadrature, i.e.  $\rho_{\rm 2Mpc+20Mpc} = \sqrt{\rho_{\rm 2Mpc}^2 + \rho_{\rm 20Mpc}^2}$ . In Figure 10, we show the posterior PDFs using the 2 Mpc rank-order distribution summary statistic of the Ly $\alpha$  forest alone (orange) and the Ly $\beta$  forest alone (purple) compared to the joint constraints

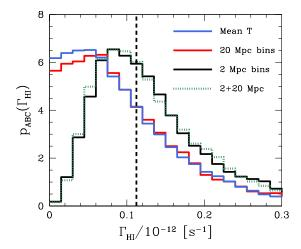


Figure 9. Posterior PDFs of  $\Gamma_{\rm H\,I}$  for the Ly $\alpha$  and Ly $\beta$  forest spectra in Figure 8 using the mean transmission (blue) versus the rank-order distribution of 2 Mpc and 20 Mpc binned transmission (red and black, respectively) as the ABC summary statistic, compared to the true value (dashed line). While the mean transmission and 20 Mpc bins only provide an upper limit to  $\Gamma_{\rm H\,I}$ , the S/N  $\sim 5.5$  2 Mpc binned spike in Ly $\beta$  is highly constraining. The green dotted curve shows the posterior PDF when the 2 and 20 Mpc rank-order distribution summary statistics are combined.

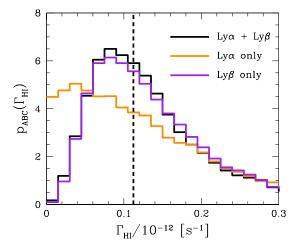
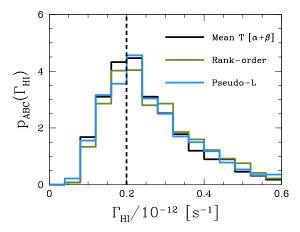


Figure 10. Posterior PDFs of  $\Gamma_{\rm H\,I}$  for the Ly $\alpha$  and Ly $\beta$  forest spectra in Figure 8 using the rank-order distribution of 2 Mpc binned transmission in Ly $\alpha$  alone (orange), Ly $\beta$  alone (purple), and both (black) as the ABC summary statistic. The dashed line indicates the true value of  $\Gamma_{\rm H\,I}$ .

(black, same as Figure 9). While the Ly $\beta$  forest has the most constraining power due to the presence of the significant transmission spike, including the *non-detection* of transmission in Ly $\alpha$  modestly improves the posterior PDF density at the location of the true  $\Gamma_{\rm H\,I}$ .

As an alternative to the rank-order distribution, we have also devised a one-dimensional summary statistic that is sensitive to rare transmission spikes which we call the "pseudo-likelihood" of the spectrum. Through forward modeling many mock data sets, we can compute the transmission PDF in our simulations to arbitrarily high precision (e.g. Fig. 4) with any set of model parameters, and then compute the "pseudo-likelihood" of the spectrum under the assumption that each bin of the Ly $\alpha$  and Ly $\beta$  forests is entirely independent:  $p(\mathbf{d}|\theta) = \prod_i P(F_i|\theta)$ .



**Figure 11.** Comparison of the ABC posterior distributions of  $\Gamma_{\rm H\,I}$  for the same mock spectrum as in Figure 6 using three different summary statistics: mean transmission (black), rank-order distribution (green), and pseudo-likelihood (blue). The true  $\Gamma_{\rm H\,I}$  is shown as the vertical dashed line.

If there were no spatial correlations in (or between) the  ${\rm Ly}\alpha$  and  ${\rm Ly}\beta$  forests, this likelihood would be exact. After finding the maximum pseudo-likelihood model parameters  $\theta_{\rm ML}$  of the observed data, we then use the absolute difference of pseudo-likelihood values in log space as the distance metric between the observed and mock data,

$$\rho(\mathbf{s}_{\text{obs}}, \mathbf{s}) = \left| \sum_{i}^{N_{\alpha+\beta}} \ln P(F_{i,\text{obs}} | \theta_{\text{ML}}) - \sum_{i}^{N_{\alpha+\beta}} \ln P(F_{i,\text{mock}} | \theta_{\text{ML}}) \right|, (6)$$

where i encompasses all of the bins in the Ly $\alpha$  and Ly $\beta$  forests and  $N_{\alpha+\beta}=N_{\alpha}+N_{\beta}$ . The pseudo-likelihood summary statistic described above is similar to "indirect inference" ABC methodologies (e.g. Drovandi et al. 2011; Gleim & Pigorsch 2013). We find that this summary statistic is equally powerful as the rank-order distribution in terms of its ability to constrain  $\Gamma_{\rm H\,I}$  from sparse transmission spikes.

Outside of examples like Figure 8, the mean transmission, rank-order distribution, and pseudo-likelihood summary statistics are comparable in their ability to constrain  $\Gamma_{\rm H\,I}$ . We demonstrate this in Figure 11 where we show ABC posterior distributions for the three statistics computed for the same mock data as Figure 6, and we have chosen the tolerance  $\epsilon$  such that we accept 5% of the 25,000 mock datasets. The rank-order distribution and pseudo-likelihood statistics should be more sensitive to additional parameters that affect the shape of the transmission PDF such as the thermal state of the IGM (e.g. Lee et al. 2015) and the strength of ionizing background fluctuations (e.g. Meiksin & White 2003). We restrict ourselves to inferring  $\Gamma_{\rm H\,I}$  alone in this work for simplicity in this initial presentation of our methodology, and we note that this choice limits the additional information gathered by the distribution of Ly $\alpha$  and Ly $\beta$  forest transmission. That is, in the models we present in this work there is a one-to-one relationship between the mean transmission and  $\Gamma_{\rm H\,I}$ , and the scale-dependent distribution of transmission does not contain much additional

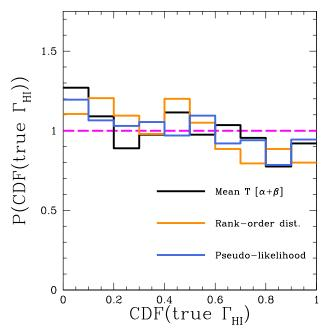


Figure 12. Inference test of the ABC methodology using the different summary statistics described in  $\S$  3.1. A total of 2000 mock measurements of  $\Gamma_{\rm H\,I}$  were performed on 2000 different mock data sets (consisting of one noisy  ${\rm Ly}\alpha+\beta$  forest spectrum covering 100 Mpc) with  $\Gamma_{\rm H\,I}=10^{-12.7}~{\rm s}^{-1}$ . The solid curves show the distribution of the posterior CDF of each mock measurement evaluated at the true  $\Gamma_{\rm H\,I}$  (i.e. CDF(true  $\Gamma_{\rm H\,I})$  as defined in the text) using the mean transmission (black), rank-order PDF (orange), and pseudo-likelihood (blue) as summary statistics.

information unless the mean transmission is close to the noise limit of the spectrum. The methodology in principle allows for measurements of other parameters, such as the strength and scale of  $\Gamma_{\rm H\,I}$  fluctuations and the thermal state of the IGM, which we will pursue in future work.

# 3.2. Validation of Statistical Methods: Inference Tests

We rigorously test the capability of ABC to perform statistical inference of  $\Gamma_{\rm H\,I}$  as follows. We conduct 2000 mock  $\Gamma_{\rm H\,I}$  measurements similar to the examples in the previous section – for each measurement, we draw one mock dataset (100 Mpc of the Ly $\alpha$  and Ly $\beta$  forests at  $z\sim 6$  with  $\Gamma_{\rm H\,I}=10^{-12.7}~{\rm s}^{-1},$  e.g. Figure 3) to be the "data", then draw 500 samples from the ABC approximate posterior distribution of  $\Gamma_{\rm H\,I}$ . For each of the 2000 mock measurements, we record the value of the cumulative distribution function (CDF), determined from the 500 posterior samples, at the true  $\Gamma_{\rm H\,I}$ , CDF(true  $\Gamma_{\rm H\,I}$ ). The procedure then results in 2000 values of CDF(true  $\Gamma_{\rm H\,I}$ ).

The simplest inference test would be to test what fraction of the time, out of the 2000 mock measurements,  $0.16 < \text{CDF}(\text{true } \Gamma_{\text{H I}}) < 0.84 \text{ (central 68\%)}, \text{ or } 0.025 < \text{CDF}(\text{true } \Gamma_{\text{H I}}) < 0.975 \text{ (central 95\%)}, \text{ etc., but we opt for a somewhat stricter test covering the entire CDF. If the ABC posterior distribution can be treated as a true probability distribution, then the probability that the true <math>\Gamma_{\text{H I}}$  lies within any interval of the CDF should be equal to the size of that probability interval, i.e.

$$P(A < \text{CDF}(\text{true } \Gamma_{\text{H I}}) < B) = B - A.$$
 (7)

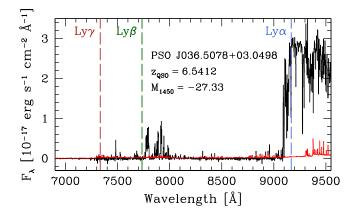


Figure 13. Keck/ESI spectrum of PSO J036.5078+03.0498 ( $z_{\rm QSO}=6.5412$ ). The spectrum (black) and noise vector (red) have been binned by six pixels ( $\approx 1$  resolution element). The wavelengths of Ly $\alpha$ , Ly $\beta$ , and Ly $\gamma$  at  $z_{\rm QSO}$  are denoted by vertical lines

In other words, the distribution of CDF(true  $\Gamma_{\rm H\,I}$ ) should follow the uniform distribution over the interval [0,1].

We demonstrate this "CDF(true  $\Gamma_{\rm H\,I}$ )" test for the mean transmission, rank order distribution, and pseudolikelihood summary statistics in Figure 12 for CDF(true  $\Gamma_{\rm H\,I}$ ) bins of width  $\Delta {\rm CDF} = 0.1$ . The dashed line shows the expected distribution of CDF(true  $\Gamma_{\rm H\,I}$ ) (i.e. a uniform distribution), while the solid curves show the distribution of CDF(true  $\Gamma_{\rm H\,I}$ ) of the 2000 mock measurements of Ly $\alpha$  and Ly $\beta$  forest spectra described above. In general, the ABC posterior distributions behave similar to the expectations for a true probability distribution, but there is a small tilt such that CDF(true  $\Gamma_{HI}$ ) tends to be < 0.5 more often than it should (i.e. P(CDF(true  $\Gamma_{\rm H\,I})$ )  $< 0.5 \sim 0.53 - 0.56$ ). This deviation from a uniform distribution is likely due to a combination of factors. First, the summary statistics may be insufficient, leading to bias in the posterior distribution. Second, the posterior PDFs from each test may not be fully converged due to the fact that  $\epsilon > 0$ , i.e. the tilt demonstrates the inherent "approximate" nature of the ABC posterior. Finally, we drew only 500 posterior samples for each test, and this may not be enough to adequately populate the tails of the posterior PDF. Nevertheless, this rigorous test shows that the probabilities from the ABC posterior distribution can be reasonably interpreted as "true" probabilities, at least in the context of our theoretical model for the IGM.

#### 4. PROOF OF CONCEPT $\Gamma_{H\,I}$ MEASUREMENT

As a proof of concept, we have applied our statistical methodology to a Keck/ESI spectrum of the recently discovered quasar PSO J036.5078+03.0498 (z=6.5412, Venemans et al. 2015b; Bañados et al. 2015, henceforth P036+03), shown in Figure 13. The quasar was observed on January 11th and 12th 2016 for a combined exposure time of 11,700s with a slit width of 1", resulting in a signal-to-noise ratio of  $\sim 20$ –45 per pixel between sky lines in the extrapolated continuum level in the Ly $\alpha$  and Ly $\beta$  forests and a spectral resolution of  $R \sim 4000$ . In the following analysis, and for the purposes of generating mock spectra, we use the noise vector from this observation instead of the one described in § 2. Further details of the data reduction and continuum fitting of

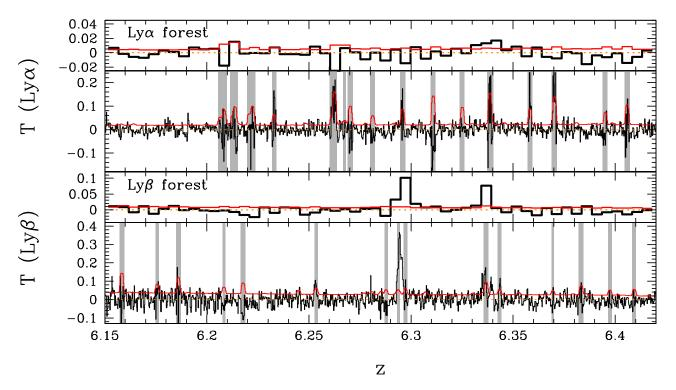


Figure 14. Overlapping Ly $\alpha$  and Ly $\beta$  forest in the highest redshift bin studied in our proof-of-concept test on P036+03. The top two panels show the Ly $\alpha$  forest, while the bottom two panels show the Ly $\beta$  forest. The lower panel in each pair shows the un-binned spectrum (black) and noise vector (red), with grey shading indicating regions with strong sky lines that we have masked in our current analysis with an automated threshold above the intra-line noise level. The upper panel in each pair shows the 2 Mpc binned spectrum (black) and noise vector (red) only including pixels outside of the masking in the lower panels.

this spectrum will be discussed in detail by Eilers et al. (in prep.). The usable Ly\$\alpha\$ forest of this quasar spans  $z \sim 5.36$ –6.42, bounded by the onset of Ly\$\beta\$ absorption at  $(1+z) = (1+z_{\rm QSO})(\lambda_{\rm Ly}_{\beta}/\lambda_{\rm Ly}_{\alpha})$  and by the \$\Delta z \sim 0.1\$ extent of the quasar proximity zone (as defined by the declining visual excess in transmission spikes, cf. Fan et al. 2006). The usable Ly\$\beta\$ forest spans  $z \sim 6.15$ –6.42, similarly cut off by the onset of Ly\$\gamma\$ absorption at  $(1+z) = (1+z_{\rm QSO})(\lambda_{\rm Ly}_{\gamma}/\lambda_{\rm Ly}_{\gamma}) = 6.15$  and by the quasar proximity zone at z = 6.42.

In Figure 14, we show a zoom-in on the overlap between the Ly $\alpha$  and Ly $\beta$  forests at  $z \sim 6.3$ . Due to the presence of correlated noise in sky lines that we currently ignore in our modeling procedure, we have automatically masked regions which have noise greater than twice the smoothly varying inter-line noise, shown as the grey vertical bands. The Ly $\alpha$  forest is nearly consistent with zero transmission, but when binned to 2 Mpc ( $\sim 20$  ESI pixels) there is a region with S/N  $\sim 3$  at  $z \approx 6.34$ . The Ly $\beta$ forest shows considerably more transmission, mostly notably a strong Ly $\beta$  spike at  $z \approx 6.295$  which is partially masked due to its overlap with sky lines. A weaker Ly $\beta$ feature also appears at  $z \approx 6.335$  which is similarly contaminated by sky lines, and may be due to the same physical structure (i.e. void in the IGM) as the Ly $\alpha$  feature at the same redshift.

We have divided the Ly $\alpha$  forest into the five redshift bins listed in Table 1. The highest redshift bin covers 108 Mpc corresponding to the entire Ly $\beta$  forest range, while the remaining four bins split the forest into 88 Mpc re-

z	$dR^a$	Ly-series	$\log \Gamma_{\rm HI}^{\rm unif}~({\rm s}^{-1})$	$\log \Gamma_{\rm HI}^{ m fluct}~({ m s}^{-1})$
6.151 – 6.418	108	$Ly\alpha+Ly\beta$	$-12.82^{+0.11}_{-0.11}$	$-12.76^{+0.23}_{-0.22}$
5.944 – 6.150	88	$Ly\alpha$	$(-12.83)^b$	$(-12.55)^b$
5.746 - 5.944	88	$Ly\alpha$	$-12.70^{+0.09}_{-0.10}$	$-12.62^{+0.23}_{-0.20}$
5.556 – 5.746	88	$Ly\alpha$	$-12.55^{+0.07}_{-0.07} \ -12.18^{+0.06}_{-0.07}$	$-12.44^{+0.21}_{-0.19}$
5.374 - 5.556	88	$Ly\alpha$	$-12.18^{+0.06}_{-0.07}$	$-12.07^{+0.22}_{-0.19}$

The reported values of  $\Gamma_{\rm H\,I}$  are the medians of the posterior PDFs, while the error bars represent the central 68% credible interval. The posterior PDFs were computed using ABC with the rank-order distribution summary statistic. Note that these uncertainties do not include systematic uncertainties due to the assumed thermal state of the intergalactic medium or the continuum fit of the quasar spectrum.

gions covering the rest of the Ly $\alpha$  forest. In each redshift bin, we perform separate ABC analyses using the three summary statistics described in § 3.1: the mean transmission, the rank-order distribution of 2 Mpc pixels, and the pseudo-likelihood of 2 Mpc pixels. The same pixels in the mock data sets were masked as in the observed spectra so as to keep the analysis of the mocks similar to what was applied to the real data. We assume a broad uniform prior on  $\Gamma_{\rm H\,I}$  from 0–3  $\times$  10<sup>-12</sup> s<sup>-1</sup> and draw 2500 samples from the (approximate) posterior PDF of  $\Gamma_{\rm H\,I}$ .

<sup>&</sup>lt;sup>a</sup> Size of redshift range in Mpc

 $<sup>^</sup>b$  95% credible upper limits.

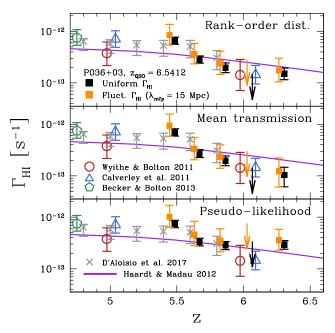


Figure 15. Proof of concept measurements of  $\Gamma_{\rm H\,I}$  from the transmission spectrum of P036+03 shown in Figure 13 divided into the bins listed in Table 1, compared to previous measurements and the commonly assumed Haardt & Madau (2012) model. The black and orange points show the median  $\Gamma_{\rm H\,I}$  of the posterior PDFs in each redshift bin assuming uniform and fluctuating ionizing background ( $\lambda_{\rm mfp}=15$  Mpc) models, respectively. Error bars denote the 16th-84th percentile range of the posterior PDFs. Where a measurement is consistent with zero, we show a downward arrow at the 95th percentile of the posterior PDF. The top, middle, and bottom panels apply the rank-order distribution, mean transmission, and pseudo-likelihood summary statistics, respectively.

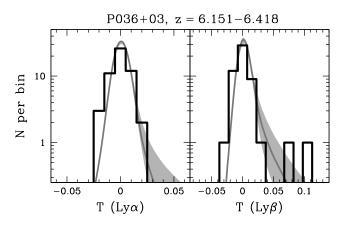


Figure 16. Transmission PDFs of the 2 Mpc-binned Ly $\alpha$  (left) and Ly $\beta$  (right) forest of P036+03 at z=6.151-6.420. The black histograms show the measured distribution of transmission for P036+03, while the grey curve and shaded regions show (fluctuating background) model PDFs corresponding to the median and 68% credible  $\Gamma_{\rm H\,I}$  values, respectively, as measured by the rank-order distribution summary statistic assuming a fluctuating ionizing background (Table 1).

Figure 15 shows the resulting  $\Gamma_{\rm H\,I}$  measurements and uncertainties compared to previous measurements. We show two limiting cases of the ionizing radiation field – a uniform background (black points), and a highly fluctuating background as suggested by DF16 at  $z\gtrsim 5.6$  (orange points). The fluctuating background models assume

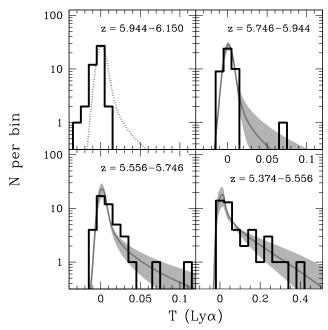


Figure 17. Transmission PDFs of the 2 Mpc-binned Ly $\alpha$  forest of P036+03 in redshift bins below the Ly $\beta$  forest overlap with corresponding (fluctuating background) model PDFs similar to Figure 16. The dotted curve in the upper left panel reflects the model PDF corresponding to the 95% credible upper limit for  $\Gamma_{\rm H\,I}$  given the lack of significantly detected transmission. Note the extended horizontal axis scale on the lower right panel.

the  $\Gamma_{\rm H\,I}/\langle\Gamma_{\rm H\,I}\rangle$  field computed as described in § 2 with  $\lambda_{\rm mfp}=15~{
m Mpc}$  (e.g. bottom panel of Figure 3, drawn from the simulation shown in Figure 2), and the constraints in Figure 15 apply to  $\langle \Gamma_{\rm H\,I} \rangle$ . In general the measurements are consistent with previous work at  $z\sim 5$ -6 (large open points; Wyithe & Bolton 2011; Calverley et al. 2011; Becker & Bolton 2013; D'Aloisio et al. 2016). These works measured  $\Gamma_{\rm H\,I}$  two different ways, either by calibrating hydrodynamical simulations to measurements of the mean transmission (Wyithe & Bolton 2011; Becker & Bolton 2013; D'Aloisio et al. 2016) or by analyzing the transmission profile of quasar proximity zones (Calverley et al. 2011). For those measurements based on the mean transmission we have adjusted their  $\Gamma_{\rm H\,I}$  values slightly to account for their different assumed cosmologies following the scaling factors in Bolton & Haehnelt (2007). Each of these measurements represents samples of  $\geq 7$  quasars, while our comparably precise measurements are from a single quasar, and we more explicitly model large-scale cosmic variance of the density field and a strongly fluctuating ionizing background. However, our stated uncertainties do not include significant systematic uncertainties considered by previous authors, which we discuss further below.

In Figure 16 we show the measured PDFs of 2 Mpc transmission (dT=0.01-binned) in the Ly $\alpha$  and Ly $\beta$  forests at z=6.151–6.420 compared to fluctuating background model PDFs corresponding to the median and 68% credible posterior values of  $\Gamma_{\rm H\,I}$  measured by the rank-order distribution (Table 1). The constraints demonstrate the capability of the ABC procedure to constrain  $\Gamma_{\rm H\,I}$  from a sparsely sampled tail of significant transmission measurements. In Figure 17 we show simi-

lar plots for the remaining lower redshift bins which are constrained by the Ly $\alpha$  forest alone. The upper left panel shows the bin of z=5.943–6.151 over which there are no significant transmission spikes detected, with the model PDF corresponding to the 95% credible upper limit on  $\Gamma_{\rm H\,I}$  shown by the dotted curve. In this redshift range, corresponding to observed wavelengths 8440–8693Å, the excess of pixels with relatively large negative transmission values compared to the model PDF suggests that there are systematics in the data reduction that are not present in our simple Gaussian noise model. The other redshift bins show good agreement between the shape of the model PDFs and the data.

The constraints from different summary statistics are nearly identical, although the pseudo-likelihood statistic leads to somewhat elevated  $\Gamma_{\rm H\,I}$  at all redshifts, most prominently in the highest redshift bin. This is likely due to our simplistic modeling of the noise in the spectrum as uncorrelated and Gaussian-distributed. In future work, we will use more realistic noise realizations extracted from real data. Both the pseudo-likelihood and mean transmission statistics are adversely affected by regions with an excess of negative transmission – which exist in the data but not in our noise model – leading to positive and negative biases in the  $\Gamma_{\rm H\,I}$  measurements, respectively.

In detail, the pseudo-likelihood statistic cannot distinguish between negative and positive outliers because the negative side of the transmission PDF is only weakly dependent on  $\Gamma_{\rm H\,I}$  (e.g. Figure 4), so excess negative transmission (wrongly) influences the posterior PDF the same way as a positive transmission spike, e.g. towards higher  $\Gamma_{\rm H\,I}$ . Conversely, excess negative transmission decreases the mean transmission more than otherwise expected by our assumed noise variations, so the inferred  $\Gamma_{\rm H\,I}$  can be biased low. Despite the presence of small-scale transmission in the Ly $\alpha$  and Ly $\beta$  forests in the highest redshift bin (Figure 14), the mean transmission in Ly $\alpha$  is consistent with zero, and the mean transmission in Ly $\beta$  is only barely detected with S/N  $\approx$  2.

Note that, for simplicity, we have not included uncertainties in the thermal state of the IGM nor uncertainties in the quasar continuum. In the case of a uniform background, the former uncertainty dominates the error budget of  $\Gamma_{\rm H\,I}$  (Becker & Bolton 2013). Preliminary tests marginalizing over a wide range in potential IGM thermal states and  $\pm 20\%$  continuum uncertainty<sup>2</sup> suggest that the true error budget should be inflated by up to  $\sim 0.2$  dex, but we leave a detailed multi-parameter analysis to future work. We have also ignored uncertainties in the mean transmission at  $z \sim 5$  which will contribute uncertainty to the Ly $\beta$  measurement – however, the uncertainty in the mean transmission is likely to be smaller than the intrinsic scatter between sightlines due to the IGM density field, which we explicitly model. Thus the uncertainties shown in Figure 15 and

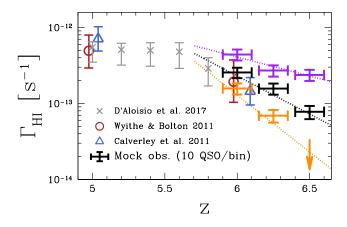


Figure 18. Purple, black, and orange error bars demonstrate the median  $\Gamma_{\rm H\,I}$  of the posterior PDF from measurements performed on mock data sets (10 quasars per bin, using the overlapping Ly $\alpha$  and Ly $\beta$  forest region) following the evolving  $\Gamma_{\rm H\,I}$  models shown by the corresponding dotted curves. The downward arrow in the highest redshift bin of the lowest  $\Gamma_{\rm H\,I}$  model represents a  $2\sigma$  upper limit from the lack of significant transmission spikes in the mock data.

listed in Table 1 should be understood as lower limits based on statistical uncertainty alone. Given our ability to measure  $\Gamma_{\rm H\,I}$  from individual sightlines, in principle we can determine how realistic our uncertainties are by comparing our predicted dispersion (from the posterior PDFs) to the actual dispersion in measurements on multiple sightlines. In future work we will directly compare our estimated uncertainties in the mean  $\Gamma_{\rm H\,I}$  to the dispersion in actual measurements from a large ensemble of quasars.

#### 5. DISCUSSION AND CONCLUSION

The  $\sim$ Mpc-scale distribution of transmission in the Ly $\alpha$  and Ly $\beta$  forests at  $z\gtrsim 6$  contains considerable statistical constraining power for the ionization state of the post-reionization IGM, but extracting this information from observed spectra is challenging. We have shown that an application of ABC should allow for precise measurements of the ionizing background at high redshift, even from  $\sim 1$  significant transmission spike in a broad spectral region.

We have demonstrated above that our method, applied to a single high-quality quasar spectrum, allows for a measurement of  $\Gamma_{\rm H\,I}$  to a precision of roughly a factor of two at z > 6 in the presence of a highly fluctuating ionizing background. This uncertainty. is dominated by cosmic variance, primarily due to the fluctuating ionizing background with a smaller contribution from density fluctuations In a fixed redshift interval, the constraining power of the Ly $\alpha$  and Ly $\beta$  forests increases roughly as  $\sqrt{N_{\rm QSO}}$ , so larger samples will not only be able to test the consistency of our uncertainty estimates but also allow for unprecedented precision in  $\Gamma_{\rm H\,I}$  measurements. The population of known  $z\gtrsim 6$  quasars has greatly increased in the last few years from all-sky surveys such as SDSS (e.g. Jiang et al. 2015) and Pan-STARRS (Venemans et al. 2015b; Bañados et al. 2016, Mazzucchelli et al., in prep.), and other ongoing searches for  $z \gtrsim 6$ quasars (e.g. Reed et al. 2015, 2017; Venemans et al. 2015a) will likely increase the potential spectroscopic

 $<sup>^2</sup>$  Due to the weak transmission at  $z\gtrsim5.5$ , uncertainties in the quasar continuum have a relatively small effect on the inferred ionizing background (see Eilers et al. 2017). In the simplest case of inference via the mean transmission,  $\Gamma_{\rm H\,I}\propto1/\tau_{\rm eff}^{\sim2.0}$  (Becker & Bolton 2013). Propagating uncertainties through  $\tau_{\rm eff}=-\ln{\langle F\rangle}$ , a continuum error of 20% implies  $\sigma_{\tau_{\rm eff}}\sim0.2$ , which then corresponds to  $\sigma_{\Gamma_{\rm H\,I}}/\Gamma_{\rm H\,I}\sim10\%$  for  $\tau_{\rm eff}\sim4$ .

sample size even further.

In Figure 18, we show mock measurements of  $\Gamma_{\rm H\,I}$  for a hypothetical survey of three samples of ten quasars each with  $z_{\rm Q}=6.25,6.50,6.75$  to measure  $\Gamma_{\rm H\,I}$  at  $z_{\rm IGM}=$ 6.00, 6.25, 6.50, respectively, using the rank-order distribution summary statistic on 100 Mpc of the overlapping Ly $\alpha$  and Ly $\beta$  forest regions. The three colors/dotted curves correspond to different toy evolution models that roughly bracket published measurements of the Ly $\alpha$  forest effective optical depth at  $z \gtrsim 6$  (Figure 1) and we assume a strongly fluctuating ionizing background ( $\lambda_{\rm mfp}$ = 15 Mpc). While we do not include them in Figure 18, at redshifts below where the Ly $\beta$  forest is cut off by the onset of Ly $\gamma$  absorption the constraints from the Ly $\alpha$ forest alone (down to  $z \sim 5.25$  for quasars at  $z_{\rm QSO} = 6$ ) would be of comparable precision.

Currently, there are  $\sim 20~z \gtrsim 6$  QSOs with moderate-resolution (e.g. Keck/ESI, VLT/X-Shooter) spectra of comparable quality (or better) to our spectrum of P036+03 in public data archives. In future work, we will perform a joint statistical analysis of all publicly available spectra of  $z\gtrsim 6$  quasars to measure  $\Gamma_{\rm H\,I}$  from  $z\sim 5.5$ to  $z \gtrsim 6.5$  and constrain IGM thermal parameters. The lower panels of Figure 4 show that background fluctuations can imprint substantial signals in the distribution of transmission in the Ly $\alpha$  and Ly $\beta$  forests on small and large scales. With a large number of independent sightlines through the IGM, it may be possible to constrain not only the mean strength of the ionizing background, but also the strength and scale of ionizing background fluctuations through a multi-scale approach.

### ACKNOWLEDGEMENTS

We thank M. Fouesneau, D. Hogg, and D. Foreman-Mackey for helpful conversations regarding statistical methods and ABC. Calculations presented in this paper used resources of the National Energy Research Scientific Computing Center (NERSC), which is supported by the Office of Science of the U.S. Department of Energy under Contract No. DE-AC02-05CH11231.

The authors wish to recognize and acknowledge the very significant cultural role and reverence that the summit of Mauna Kea has always had within the indigenous Hawaiian community. We are most fortunate to have the opportunity to conduct observations from this mountain.

# REFERENCES

- Almgren, A. S., Bell, J. B., Lijewski, M. J., Lukić, Z., & Van Andel, E. 2013, ApJ, 765, 39
- Bañados, E., Decarli, R., Walter, F., et al. 2015, ApJ, 805, L8 Bañados, E., Venemans, B. P., Decarli, R., et al. 2016, ArXiv e-prints, arXiv:1608.03279
- Barnett, R., Warren, S. J., Becker, G. D., et al. 2017, ArXiv e-prints, arXiv:1702.03687
- Beaumont, M. A., Cornuet, J.-M., Marin, J.-M., & Robert, C. P. 2009, Biometrika, doi:10.1093/biomet/asp052
- Becker, G. D., & Bolton, J. S. 2013, MNRAS, 436, 1023
- Becker, G. D., Bolton, J. S., Madau, P., et al. 2015, MNRAS, 447, 3402
- Becker, G. D., Rauch, M., & Sargent, W. L. W. 2007, ApJ, 662,
- Becker, R. H., Fan, X., White, R. L., et al. 2001, AJ, 122, 2850
- Bolton, J. S., & Becker, G. D. 2009, MNRAS, 398, L26
- Bolton, J. S., & Haehnelt, M. G. 2007, MNRAS, 382, 325
- Calverley, A. P., Becker, G. D., Haehnelt, M. G., & Bolton, J. S. 2011, MNRAS, 412, 2543

- Cameron, E., & Pettitt, A. N. 2012, MNRAS, 425, 44
- Chornock, R., Berger, E., Fox, D. B., et al. 2014, ArXiv e-prints, arXiv:1405.7400
- 2013, ApJ, 774, 26
- D'Aloisio, A., McQuinn, M., Davies, F. B., & Furlanetto, S. R. 2016, ArXiv e-prints, arXiv:1611.02711
- D'Aloisio, A., McQuinn, M., & Trac, H. 2015, ApJ, 813, L38 Davies, F. B., & Furlanetto, S. R. 2016, MNRAS, 460, 1328
- Drovandi, C. C., Pettitt, A. N., & Faddy, M. J. 2011, Journal of the Royal Statistical Society: Series C (Applied Statistics), 60,
- Eilers, A.-C., Hennawi, J. F., & Lee, K.-G. 2017, ApJ submitted Fan, X., Narayanan, V. K., Strauss, M. A., et al. 2002, AJ, 123, 1247
- Fan, X., Narayanan, V. K., Lupton, R. H., et al. 2001, AJ, 122, 2833
- Fan, X., Strauss, M. A., Schneider, D. P., et al. 2003, AJ, 125, 1649
- Fan, X., Strauss, M. A., Becker, R. H., et al. 2006, AJ, 132, 117 Field, G. B. 1959, ApJ, 129, 525
- Furlanetto, S. R., Zaldarriaga, M., & Hernquist, L. 2004, ApJ,
- Gleim, A., & Pigorsch, C. 2013, Draft paper: http://ect-pigorsch. mee. uni-bonn. de/data/research/papers
- Goto, T., Utsumi, Y., Hattori, T., Miyazaki, S., & Yamauchi, C. 2011, MNRAS, 415, L1
- Gunn, J. E., & Peterson, B. A. 1965, ApJ, 142, 1633
- Hahn, C., Vakili, M., Walsh, K., et al. 2016, ArXiv e-prints, arXiv:1607.01782
- Ishida, E. E. O., Vitenti, S. D. P., Penna-Lima, M., et al. 2015, Astronomy and Computing, 13, 1
- Jennings, E., & Madigan, M. 2016, ArXiv e-prints, arXiv:1608.07606
- Jiang, L., McGreer, I. D., Fan, X., et al. 2015, AJ, 149, 188 Lee, K.-G., Hennawi, J. F., Spergel, D. N., et al. 2015, ApJ, 799,
- Lidz, A., Heitmann, K., Hui, L., et al. 2006, ApJ, 638, 27 Loeb, A., & Furlanetto, S. R. 2013, The First Galaxies in the Universe
- Lukić, Z., Stark, C. W., Nugent, P., et al. 2015, MNRAS, 446, 3697
- Lusso, E., Worseck, G., Hennawi, J. F., et al. 2015, MNRAS, 449,
- Marin, J.-M., Pudlo, P., Robert, C. P., & Ryder, R. J. 2012, Statistics and Computing, 22, 1167
- McGreer, I. D., Mesinger, A., & D'Odorico, V. 2015, MNRAS, 447, 499
- McGreer, I. D., Mesinger, A., & Fan, X. 2011, MNRAS, 415, 3237
- Meiksin, A., & White, M. 2003, MNRAS, 342, 1205
- Mesinger, A., & Furlanetto, S. 2007, ApJ, 669, 663 Mortlock, D. J., Patel, M., Warren, S. J., et al. 2009, A&A, 505,
- Oh, S. P., & Furlanetto, S. R. 2005, ApJ, 620, L9
- Planck Collaboration, Aghanim, N., Ashdown, M., et al. 2016a, ArXiv e-prints, arXiv:1605.02985
- Planck Collaboration, Adam, R., Aghanim, N., et al. 2016b, ArXiv e-prints, arXiv:1605.03507
- Pritchard, J. K., Seielstad, M. T., Perez-Lezaun, A., & Feldman, M. W. 1999, Molecular Biology and Evolution, 16, 1791
- Reed, S. L., McMahon, R. G., Banerji, M., et al. 2015, MNRAS, 454, 3952
- Reed, S. L., McMahon, R. G., Martini, P., et al. 2017, ArXiv e-prints, arXiv:1701.04852
- Rollinde, E., Theuns, T., Schaye, J., Pâris, I., & Petitjean, P. 2013, MNRAS, 428, 540
- Sheinis, A. I., Bolte, M., Epps, H. W., et al. 2002, PASP, 114, 851 Songaila, A. 2004, AJ, 127, 2598
- Tang, J.-J., Goto, T., Ohyama, Y., et al. 2016, ArXiv e-prints, arXiv:1612.06148
- Venemans, B. P., Verdoes Kleijn, G. A., Mwebaze, J., et al. 2015a, MNRAS, 453, 2259
- Venemans, B. P., Bañados, E., Decarli, R., et al. 2015b, ApJ, 801, L11
- White, R. L., Becker, R. H., Fan, X., & Strauss, M. A. 2003, AJ,
- Willott, C. J., Delorme, P., Omont, A., et al. 2007, AJ, 134, 2435

Worseck, G., Prochaska, J. X., O'Meara, J. M., et al. 2014, MNRAS, 445, 1745

Wyithe, J. S. B., & Bolton, J. S. 2011, MNRAS, 412, 1926